Packings and defects of strongly coupled two-dimensional Coulomb clusters: Numerical simulation

Ying-Ju Lai and Lin I
Department of Physics, National Central University, Chungli, Taiwan 32054, Republic of China
(Received 29 March 1999)

The packings and defects of the strongly coupled two-dimensional Coulomb clusters with particle number N from a few to a few hundred with different forms of mutual repulsion and central confining potentials at zero temperature are investigated using molecular-dynamics simulation through many annealing cycles. The circular symmetry of the confining potential and the interplay with the mutual repulsion lead to the strong competition between the outer circular shells and the inner triangular lattice. Generic packing behaviors, such as the concentric shells with the classical periodic packing sequence at small N, and the triangular latticelike inner core surrounded by a few outer circular shells at large N are observed. The effects of changing the interaction and confining potentials on the detailed packing sequence, the radial variation of packing density, and the positions of the shell-triangular core interface are investigated with a detailed study of the cluster structures along with the formation and distribution of topological defects. [S1063-651X(99)03410-8]

PACS number(s): 52.90.+z, 45.05.+x, 61.46.+w, 73.23.−b

I. INTRODUCTION

The two-dimensional strongly coupled Coulomb cluster (2D SCCC) with a few to a few hundred charged particles through Coulomb-type interactions is a fundamental model system to test the behaviors of the finite N (particle number) limit of the 2D Wigner crystal, which has a triangular lattice at $N=\infty$. The electron dimples on the liquid-helium surface, the electrons in the 2D semiconductor Coulomb blockades, and the flux lines in the superfluids, superconductor, and magnetoplasma systems are the few similar systems [1–5]. Usually, in a circular confinement cell, a radial force generated by the external confinement or the neutralizing background is needed to confine particles with repulsive interaction. The packing of the clusters at different particle number N is determined by the interplay between the confining and repulsion forces. The early theoretical work by Thomson in his *raisin model* for the *classical atoms* with electrons imbedded in a uniform neutralizing ion background [6] and several recent theoretical and numerical studies reported some generic packing behaviors [7–12]. The competition between the triangular lattice for an infinite 2D system and the shell structure due to bending by the central confining force leads to the clusters with interesting self-organized patterns which show concentric shells at small N and triangular cores surrounded by the circular outer shells at large N. Defects are present to accommodate the bending and other lattice deformation. A packing sequence with Mandeleev tables for the occupation numbers in different shells up to $N=230$ with $1/r^2$ repulsive force in a parabolic potential and an example in a square potential have also been predicted by the Monte Carlo (MC) simulations [7]. Similar analytical results of the packing sequences under other more general interaction forms such as with $1/r^n$ repulsive force ($n=1$, 2, and 3) in a parabolic confining well (with a few tens particles) and with $1/r^2$ repulsive force in a r^m confining well ($m=1$, 2, 3, and 10 and N from 2 to 24) [11], and the numerical results of the ground-state configurations at $N=30$ with a few different Debye lengths for the Yukawa-type interaction in a parabolic confining well and the transition to the Wigner crystals at small Debye length, were also reported [12].

Recently, the formation of the quasi-2D large volume triangular Coulomb lattice with negatively charged μm-sized dust particles (10^4 electrons/particle) suspended in weakly ionized plasmas was demonstrated [13–15]. We further designed a small cylindrical plasma trap for confining the quasi-2D dust Coulomb clusters and provided a systematic experimental support for the above generic packing behaviors from small to large N [16,17], although the occupation numbers might deviate slightly and the interactions in our real plasmas are more complicated than the previous simple models [7,9]. Obviously, some universal features are shared and the detailed interaction forms can cause differences on the particle packing and defect configurations. In this work, using molecular-dynamics (MD) simulations for the examples with a few typical interaction forms, we study to what extent the generic rules are obeyed and the effect of the interaction forms on the details such as the packing sequences, structures of the ground and nearly degenerated metastable states, radial distribution of lattice constant, etc., for the packing of 2D SCCC's from small to large N up to a few hundreds at zero temperature. Unlike some of the previous analytical and numerical studies mainly focusing on the energies and packing sequences of the ground states, the collective excitation spectra, and the phase transition [7–12], we further use the idea of defects to get a better understanding of the topological nature of the cluster structures, and study the general behaviors of the defects under the circular bending and nonuniform lattice constant distribution, such as N, interaction forces, and confining potential change.

For a 2D cluster with particles in a central confining field and repulsive mutual interactions, the potential V_i of the ith particle with radius distance r_i can be expressed as

$$V_i = V_c(r_i) + \sum_{j=1, j\neq i}^{N} V_{ij}(r_{ij}),$$

 © 1999 The American Physical Society

where $V_c(r_i)$ is the confining potential and the next term comes from the repulsions from other particles in the cluster with interparticle separation r_{ij}. Usually, the former increases monotonically with r_i and the latter decreases monotonically with increasing separation. The packing is a consequence of the competition between them to minimize the total energy of the system. The generic packing behavior can be easily understood through the following picture. If we start from the extreme case of hard spheres in a parabolic well with a weak central confining force, the triangular packing shown in Figs. 1(a)–1(d) with one to four particles at the center is the basic configuration for the structure of the cluster core, because there is no way to compress the hard spheres. Changing the total particle number N may cause the change of the detailed shape of the boundary and shifting the position of the center of mass of the cluster relative to the position of the vertex of the lattice associated with changing the occupation number of the center core [9]. For a uniform magic packing, the difference between the occupation numbers of the two adjacent shells should be six [e.g., Figs. 1(b)–1(e)]. There are six topological defects each with -1 topological charge sitting at the six corners of each cluster. The particles around the corners of the hexagon are far from the center and cost too much V_c. Especially when the particle number N is large, they might move from the corner to the straight sides to reduce energy. If the hard-sphere interaction can be softened, their positions can be readjusted. Concentric shells with the shape between the circular and the hexagonal shapes can be formed [e.g., Fig. 1(f)]. For certain nonmagic configurations, the deformation may also induce the formation of defects in the cluster core or even with five particles in the first shell. The rise of the strain energy due to the lattice deformation can be compensated by the reduction of the confining potential. As N increases, the addition of one particle into a certain shell increases the interparticle separation in the adjacent shell and provides space for inserting the next particle. Therefore, unlike the *quantum atoms* in which new electrons are only present in the outer shells, the occupation number in different shells can alternately change as N increases. A new shell can also be generated after all the existing shells are full. The detailed forms of V_c and V_{ij} determine how easy the triangular lattice can be deformed to minimized the total energy. Depending on the interaction forms, classical periodic tables controlling the packing sequence can be constructed.

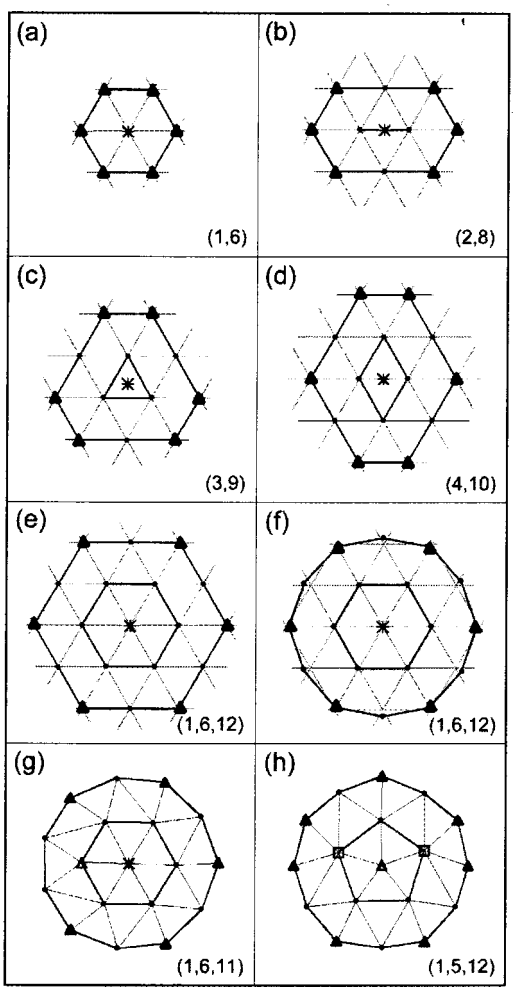

FIG. 1. (a)–(e) The sketches of the basic packing configurations with one to four particles at the center shell for the extreme case of hard-sphere interactions (left column) in a weak confining field. The triangular lattice in the background is plotted as a reference. The star represents the center of mass of the system. Depending on the occupation number of the center shell, it can sit at the vertex, the middle point between two vertexes, and the center of the center triangle. There are six -1 topological charges (threefold disclination defects) marked by the six solid triangles at the six corners of each hexagon (note that the defect-free site along a straight lattice boundary should have four nearest neighbors). (f) Softening the mutual repulsion causes the formation of the more circular outmost shell. Removing one particle from one corner of the (1,6,12) state in (e) and adjusting the interaction potential can generate the (1,6,11) state [(g)] or (1,5,12) state [(g)] with defects present in the inner part but still conserved total topological charges. The $+1$ (sevenfold) and -1 (fivefold) defects are marked by open squares and triangles, respectively.

II. NUMERICAL METHOD

In our MD simulation, the equation of motion of the ith particle (α direction) follows:

$$\frac{d^2x_{\alpha i}}{dt^2} = -\frac{\partial V_i}{\partial x_{\alpha i}} - \gamma \frac{dx_{\alpha i}}{dt} + \eta(x_{\alpha i}, t),$$

where the mass and the coefficient of the leading term (r_i^2 term) of V_c are normalized to 1. $-\gamma(dx_{\alpha i}/dt)$ corresponds to the linear viscous damping to extract kinetic energy to the background and η is the spatially and temporally δ-correlated Gaussian noise with zero mean to simulate background fluctuations. All the physical quantities are dimensionless. The fourth-order Runge-Kutta method is used to obtain the time evolution to the static state. Many cycles of annealing processes by slowly rising and then decreasing the intensity of noise (i.e., system temperature) to zero are conducted to find the ground and metastable states. Comparing with the previous work using MC simulation for the case of $V_c = r_i^2$ and $V_{ij} = 1/r_{ij}$, same ground-state packing sequence and energies are obtained [7]. This MD program is also applied in our study for the dynamical behaviors of various excitations at finite temperature. The details will be presented soon.

In our study, several different interaction forms are used to find the equilibrium states in a parabolic confining well at zero temperature. For the Yukawa-type interaction, the effect of changing Debye length λ_D is checked. $\lambda_D=\infty$ corresponds to the case of unshielded charged particles on a flat 2D surface. We also test the case with $V_{ij}=\ln(1/r_{ij})$, which is the interacting potential between two uniformly charged infinite long lines i and j to simulate the ideal 2D Coulomb interaction. Note that in the ideal 2D case (i.e., with a uniform axial charge distribution), the parabolic confining potential is equivalent to the field generated by a uniform frozen neutralizing ion background. The cases with a fourth power term added on the parabolic confining potential are also tested to check the effect of the steeper confining potential in the outer region of the clusters, which might occur for the case of confining charged dust particles by the space charge field in our experimental plasma system [16]. The degrees of lattice bending for forming a circular outer shell and the local adjustment to match the interface between the inner triangular domain and outer circular shells are manifested by the presence of the disclination defects with $+1$ and -1 topological charges (represented by squares and triangles, respectively, in the corresponding figures in this paper).

III. RESULTS AND DISCUSSIONS

A. Packing sequence at small N

For a cluster at small N, particles are packed into concentric shells. Table I shows the packing sequences of the ground states for several different interaction forms. The typical cluster structures are also shown in Figs. 2–4. The state $(N_1,N_2,N_3,\ldots)$ corresponds to the state with occupation number N_i in the ith shell from the center. Increasing N one by one causes the variation of N_i. A new shell appears when the existing shells are full.

First we start from the example of the ideal 2D Coulomb system with $V_{ij}=\ln(1/r_{ij})$ in a parabolic V_c (Table I, type-IV interaction). For $N=3$, 4, and 5, polygons are formed. For $N=6$, a particle appears at the center of the pentagon to minimize energy and forms the two-shell structure. Namely, a single shell structure with $N_1=6$ is not allowed because it costs too much confining energy. The states with (1,6), (1,7), (1,8), and (2,8) structures are found as N increases from 7 to 10. Further increasing N to 16 causes the alternate increase of N_1 and N_2 until both shells are full (i.e., $N_1=5$ and $N_2=11$). For $N=17$, the third shell appears. It forms the (1,5,11) structure. For the structure with three shells, similar filling processes are observed. The occupation number difference between the adjacent shells, $\Delta N_i=N_{i+1}-N_i$, usually varies between 5 and 6. It can change to 4 or 7 around the transition of increasing one extra shell. Note that many nearly degenerate metastable states have also been observed (see the examples in Figs. 3 and 4).

For the cases of Yukawa-type interaction $V_{ij}=\exp(-r_{ij}/\lambda_D)/r_{ij}$, which has a shorter interaction range and harder repulsive core for each particle at small λ_D, similar packing results are obtained. The results from the three representative cases with $\lambda_D=0.1$, 1, and ∞ are presented in Table I (the type-I, -II, and -III interactions, respectively). The ground-state configurations for the case of $\lambda_D=\infty$ are shown in Fig. 2. The harder repulsive core with the shorter-range interaction makes N_i deviate from those of the $\ln(1/r_{ij})$ interaction for certain cases. It tends to have a smaller cluster with the inner core, which has higher packing density. It might also change the ground-state configuration. For example, in the case of $V_{ij}=1/r_{ij}$ (i.e., $\lambda_D=\infty$), the (1,8) state which is the stable state for $V_{ij}=\ln(1/r_{ij})$ becomes metastable and the state (2,7) becomes the new ground state. The old ground states (5,11), (1,7,14), (1,8,14), (3,8,14), (3,9,15), (4,9,15), and (4,10,16) become metastable and are replaced by the new ground states (1,5,10), (2,8,12), (2,8,13), (3,9,13), (4,9,14), (4,10,14), and (5,10,15), respectively. Namely, ΔN_i might decrease by one or two. Note that usually the energy differences between the above ground and metastable states are very small ($<0.05\%$). Table I shows that decreasing λ_D from ∞ to 0.1 tends to further decrease ΔN_i by one for some configurations.

TABLE I. The Mendeleev table for the particle packing sequences from $N=1$ to 30 under defferent combinations of the confining and the mutual repulsion potentials. I to V are also used in other figures to represent the corresponding type of interaction and confinement. r_{cN} used in the type-V confining potential is the cluster radius obtained in the type-III interaction at the corresponding N.

V_c	r_i^2				$r_i^2+r_i^4/r_{cN}^2$	
V_{ij}	$\exp(-r_{ij}/\lambda_D)/r_{ij}$					
N	$\lambda_D=0.1$	$\lambda_D=1.0$	$\lambda_D=\infty$	$\ln(1/r_{ij})$	$1/r_{ij}$	Expt.
3	3	3	3	3	3	3
4	4	4	4	4	4	4
5	5	5	5	5	5	5
6	1,5	1,5	1,5	1,5	6	1,5
7	1,6	1,6	1,6	1,6	1,6	1,6
8	1,7	1,7	1,7	1,7	1,7	2,6
9	2,7	2,7	2,7	1,8	1,8	2,7
10	2,8	2,8	2,8	2,8	2,8	2,8
11	3,8	3,8	3,8	3,8	2,9	3,8
12	3,9	3,9	3,9	3,9	3,9	3,9
13	4,9	4,9	4,9	4,9	3,10	4,9
14	4,10	4,10	4,10	4,10	4,10	4,10
15	5,10	5,10	5,10	4,11	4,11	5,10
16	1,5,10	1,5,10	1,5,10	5,11	5,11	5,11
17	1,6,10	1,6,10	1,6,10	1,5,11	5,12	1,5,11
18	1,6,11	1,6,11	1,6,11	1,6,11	1,5,12	1,6,11
19	1,6,12	1,6,12	1,6,12	1,6,12	1,6,12	1,6,12
20	1,7,12	1,7,12	1,7,12	1,7,12	1,6,13	1,7,12
21	2,7,12	2,7,12	1,7,13	1,7,13	1,7,13	1,7,13
22	2,8,12	2,8,12	2,8,12	1,7,14	1,7,14	2,7,13
23	3,8,12	3,8,12	2,8,13	1,8,14	1,8,14	2,8,13
24	3,8,13	3,8,13	3,8,13	2,8,14	2,8,14	2,8,14
25	3,9,13	3,9,13	3,9,13	3,8,14	2,8,15	3,8,14
26	4,9,13	4,9,13	3,9,14	3,9,14	3,9,14	3,9,14
27	4,9,14	4,9,14	4,9,14	3,9,15	3,9,15	3,9,15
28	4,10,14	4,10,14	4,10,14	4,9,15	3,9,16	4,9,15
29	4,10,15	5,10,14	4,10,15	4,10,15	3,10,16	4,10,15
30	5,10,15	5,10,15	5,10,15	4,10,16	4,10,16	4,10,16
	I	II	III	IV	V	VI

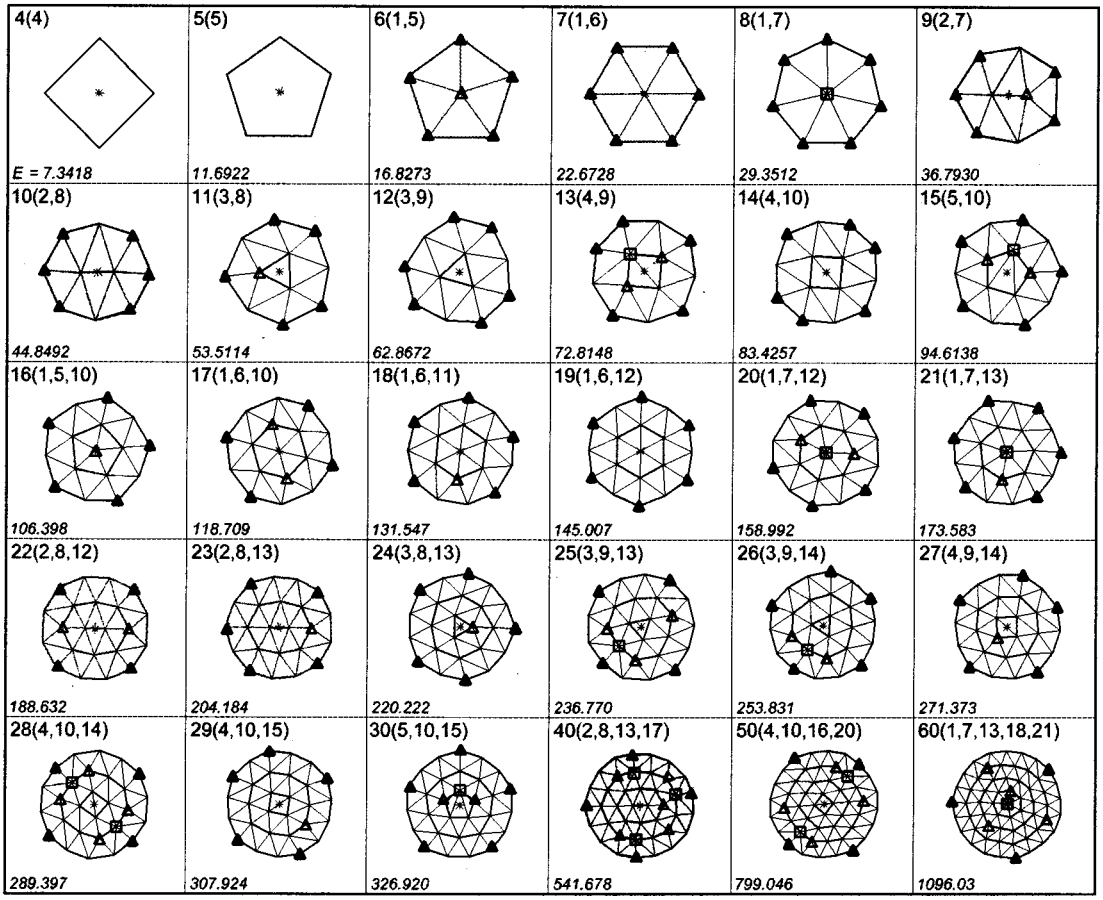

FIG. 2. The typical ground states at different N up to 60 with type-III interaction and confining potentials as defined in Table I. For displaying purposes, the scales are not the same for the clusters [see Fig. 9(c) for the mean lattice constant]. The center of mass of each cluster is represented by the star. The total dimensionless energy is listed below each cluster. The $+1$ and -1 topological defects are represented by the small squares and triangles, respectively. The solid symbols are the corresponding defects along the cluster boundary.

We also test the effect of the confinement with a steeper potential in the outer region, $V_c(r_i)=r_i^2+r_i^4/(r_{cN})^2$ (see Table I, type-V interaction), where r_{cN} is the radius of the type-III cluster at the corresponding N. It corresponds to the case with an extra nonuniform neutralizing background concentrated mainly around the cluster boundary, which generates larger confining force. Similar to the generic behaviors of other interactions, alternate packing in concentric shells is obtained. For example, many states identical to those found in the case of $V_{ij}=\ln(1/r_{ij})$ and $V_c(r_i)=r_i^2$ can be recovered and for some configurations ΔN_i can even be larger by 1. The stronger compression due to the extra steeper confining in the outer region increases N_i (i.e., the packing density) in the outer region. Note that in this case, the single shell state with six particles at $N=6$, which never occurs in other cases, is observed. Similar behavior of increasing the packing density in the outer region was also observed for the case of $V_{ij}=1/r_{ij}$ and $V_c(r_i)=r_i^n$ as n increases [11].

It is interesting to note that although packing into concentric shells was predicted by Thomson's analytical method, the analytical and the numerical results are not exactly the same. The packing sequence and the ground-state energies from our MD simulation for the case of $V_{ij}=1/r_{ij}$ and $V_c=r_i^2$ are the same as those predicted by the MC simulation [7] but are slightly different from those obtained based on the analytical Thomson's method [11]. Our packing sequence for the case of $V_{ij}=\ln(1/r_{ij})$ and $V_c=r_i^2$ is also slightly different from that obtained from the analytical Thomson's method [11].

B. Structures and defects at small N

The triangular lattice is the most stable structure for the infinite large 2D system. However, the central confining force tries to bend the lattice. The bending causes large strain energy, especially when the cluster size is small. Figure 2 shows the ground-state structures for the case of $V_{ij}=1/r_{ij}$ and $V_c(r_i)=1/r_i^2$. For the two-shell clusters with two, three, and four particles in the first shell, the shape of the second shell is between a circle and a polygon connecting the triangular lattice sites. For example, for the (2,8) structure, the second shell is elliptical due to the elongated center core. However, for the three-shell cluster, the outmost shell is almost circular even though the core is elongated.

We can also use defects to classify the topology and understand the packing problem. Starting from a perfect triangular lattice, each particle should be surrounded by its six nearest neighbors. The sites surrounded by seven and five nearest neighbors are called sevenfold and fivefold disclination defects (represented by the open squares and triangles in

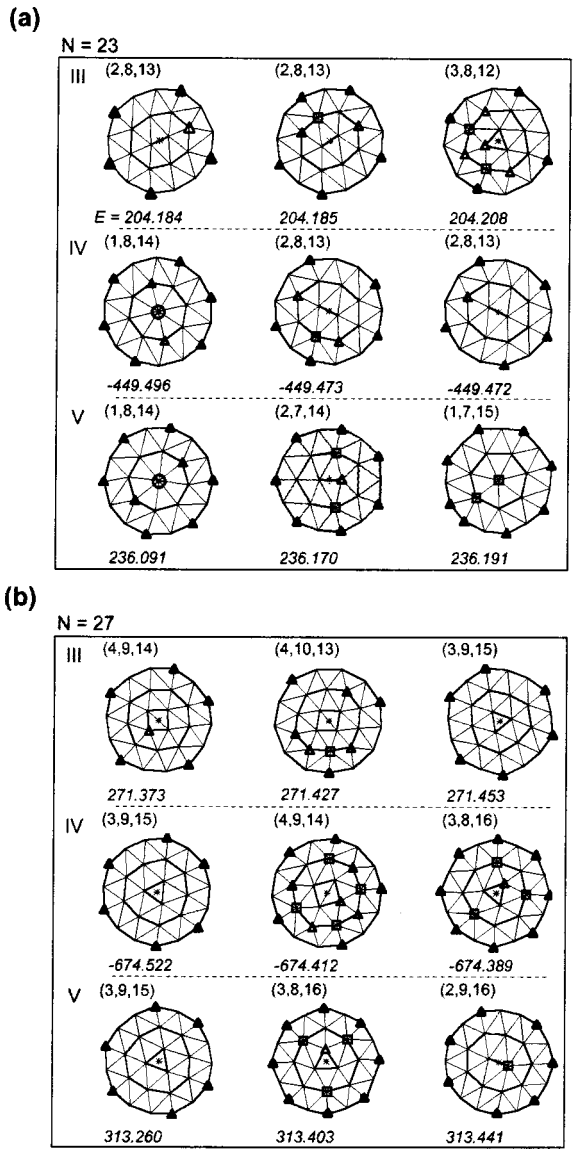

FIG. 3. The ground (first column) and nearly degenerated metastable states at $N=23$ and 27 under the type-III, -IV, and -V interaction and confining forms as defined in Table I. The triangles and squares correspond to the $+1$ and -1 topological defects, respectively. The circle at the center of the (1,8,14) state corresponds to the $+2$ topological defect. The energy (dimensionless) is listed below each cluster. Note that the system can also be locked in the metastable states without the change of occupation numbers but only the change of the relative intershell angular positions and the defect configurations.

all the figures showing the structures) associated with $+1$ and -1 topological charge, respectively [18]. Similarly, along the straight boundary of a perfect triangular lattice, each particle has four nearest neighbors. The fivefold and threefold disclination defects (represented by the solid squares and triangles, respectively, in our corresponding figures) along the boundary of a bent lattice have $+1$ and -1 topological charges, respectively. The presence of the $+1$ (-1) disclination defect causes the lattice lines to be concave toward (bend around) the defect center. For the extreme case of the hard-sphere interaction, each magic packing such as (1,6), (2,8), (3,9), (4,10), (1,6,12), (2,8,14), (3,9,15), (4,10,16), etc., has a defect-free core and six threefold defects at the six corners of the outmost hexagon (see Figs. 1–3). The net topological charge is -6. Rounding the outmost shell but still keeping the same magic packing through changing interaction forms causes no change on the defect configuration [e.g., the (3,9,15) clusters in Fig. 3(b)]. However, if the packing is no longer magic due to the change of interaction forms or N, the defects could move away from the outmost shell (Figs. 2–4) but the total topological charge is still conserved. For example, simply removing one particle from a corner of the outmost shell in Fig. 1(e) shifts one -1 defect to the second outmost shell. The (1,6,11) cluster with circular outmost shell but the same defect configuration or the (1,5,12) structure with different defect configuration but the same total topological charges can be obtained when the hard-sphere interaction is further softened and particle positions are locally adjusted [Figs. 1(g) and 1(h)]. In addition to the isolated fivefold defect with -1 topological charge, defects could also appear in the form as 5-7 pairs (i.e., free dislocations with no net topological charge) to accommodate lattice deformation. The opposite lattice bendings by the 5- and 7-defects cancel each other. It mainly introduces extra lattice lines and deteriorates the translational order, but not the orientational order. However, other defect clusters such as 5-7-5 and 7-5-7 with net topological charge deteriorate both orders. For those states such as (2,8,13), (3,9,14), (4,10,15), etc., which have magic inner cores, the defects only stay around or outside the magic core boundaries. The total topological charges on the outmost shell equal $-\Delta N_i$ for the outmost shell. One or two negative topological charges can move from the cluster boundary (core) to the core (cluster boundary) for those clusters with higher (lower) packing density in the core. For example, there are seven fivefold defects in the outmost shell and one sevenfold defect in the core for the (2,9,16) structure shown in the lowest row of Fig. 3(b).

The clusters support nearly degenerate metastable states with very small energy difference. Figures 3 and 4 show a few examples under different interaction forms and N. The states in the first column of Fig. 3 are the ground states (e.g., comparing the energy listed below each cluster). In addition to the states with different N_i at the same N [e.g., (2,8,13) and (3,8,12) at $N=23$ in Fig. 3(a) and other states at $N=27$ in Fig. 3(b)], other nearly degenerate metastable states can also be found with the same N_i but different defect configurations. For example, comparing the two different (2,8,13) states in the first row of Fig. 3(a), the slightly different relative positions between the particles in the adjacent shells can lock the system into different metastable states. At finite temperature, the thermally excited intershell angular vibration around the locked state and the intershell angular hopping associated with defect generation and hopping to different locked states were experimentally observed [16,17]. However, it is more difficult to excite the radial hopping which causes the changes of N_i due to the higher-energy barrier unless a high temperature is reached. The numerical details will be presented in the future.

Increasing the steepness of the repulsive core of V_{ij} makes the bending to a circular outmost shell harder. The cluster structure is more similar to the hard-sphere packing with triangular lattice and facets around cluster boundary at the small λ_D limit. This trend was also reported in the pre-

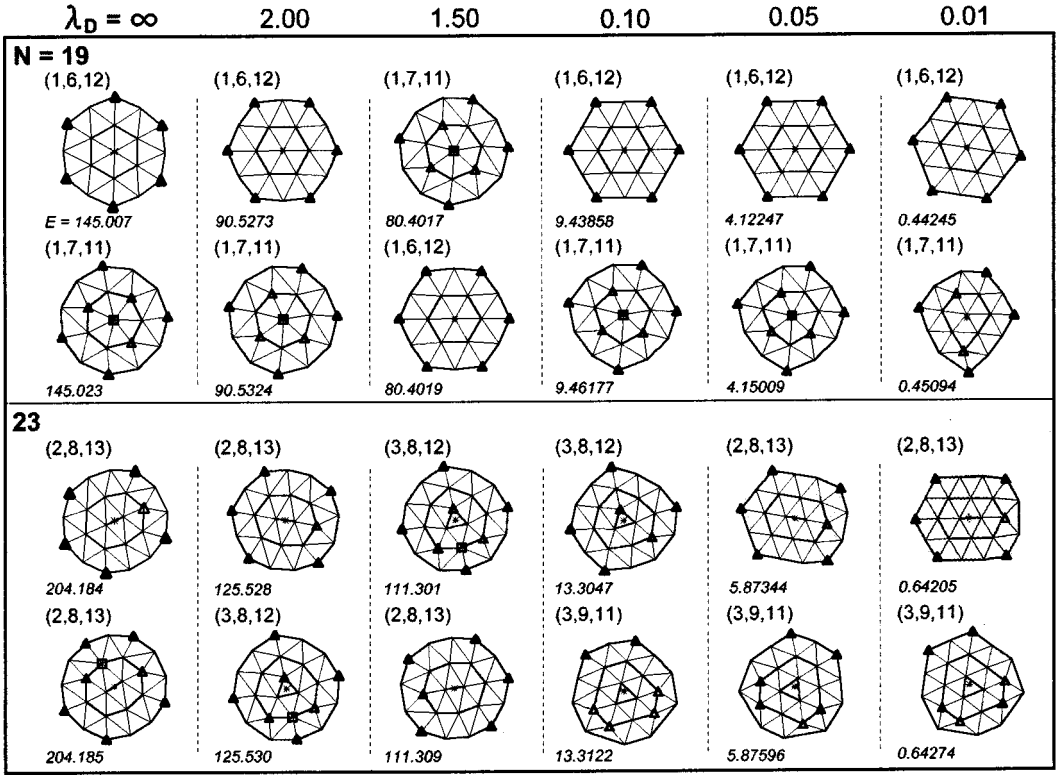

FIG. 4. The evolution of the ground and the nearest metastable states at $N=19$ and 23 for the Yukawa-type repulsion in a parabolic confining well with decreasing λ_D (dimensionless). At the small λ_D limit, the outmost shell becomes more similar to the triangular packing of the hard sphere. The dimensionless energy of each state is listed below each cluster.

vious numerical simulation at $N=30$ [12]. As shown in Fig. 4, the series of the ground-state (the first and the third rows) and the metastable-state configurations starting from the (1,6,12) and (2,8,13) states at $N=19$ and 23, respectively, with the gradual decrease of λ_D to very small values, gives two typical examples. Especially, the latter has an interesting structure with an elongated core. The (1,6,12) and (2,8,13) states remain the ground states over most of the range of λ_D except that in a middle narrow window they are replaced by the nearly degenerate states (1,7,11) and (3,8,12), respectively. Note that the former two states have defect-free cores which have lower strain energies than the latter two states, which have more defects. In both cases, the mean lattice constant a remains almost constant ($1.01 \geqslant a \geqslant 0.99$) for $\infty > \lambda_D > 5$, and then slowly decreases with decreasing λ_D (Fig. 5). As the repulsive potential becomes steeper with the decreasing λ_D (see the inset in Fig. 5), the more difficult compression makes the outmost shells less circular, especially for the (1,6,12) and (2,8,13) states. The particles around the long ends or the corners of their outmost shells cost too much confining energies. Therefore, the (1,7,11) and (3,8,12) states which have more circular outer shells become the ground states. However, in the case of very small λ_D, the repulsive core becomes very hard and small. The whole cluster sits in the center flatter region of the parabolic well. The decrease of the total strain energy due to the fewer defects of the (1,6,12) and (2,8,13) states than the (1,7,11) and (3,8,12) states can pay off the small increase of the confining potential due to the deviations from the circular outmost shell.

C. Structures and defects at large N

For the clusters at large N, it is easier to bend the outer lattice to form circular shells. Clusters with triangular-lattice-like core surrounded by the more circular outmost shells are obtained. Figures 6–8 show a few typical configurations with increasing N up to a few hundred. The number of the circular outer shells increases to about two when N reaches about one hundred. This agrees with the previous MC simulation re-

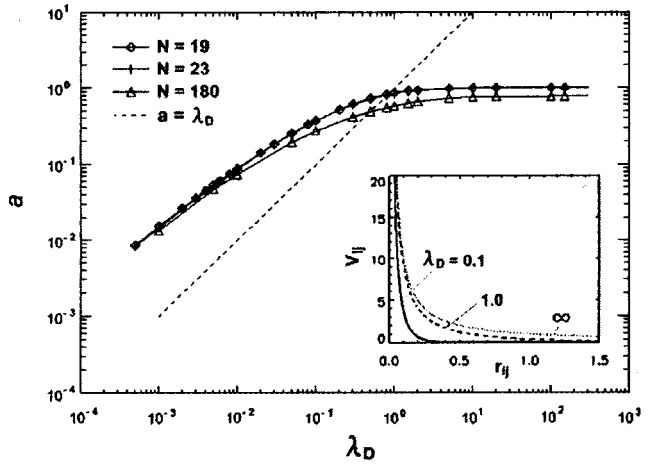

FIG. 5. The variations of the mean lattice constant a vs λ_D for the Yukawa repulsions in a parabolic confining well at $N=19$, 23, and 180. It is hard to distinguish the curves for $N=19$ and 23. The inset shows the radial dependences of a few typical confining potentials at different λ_D.

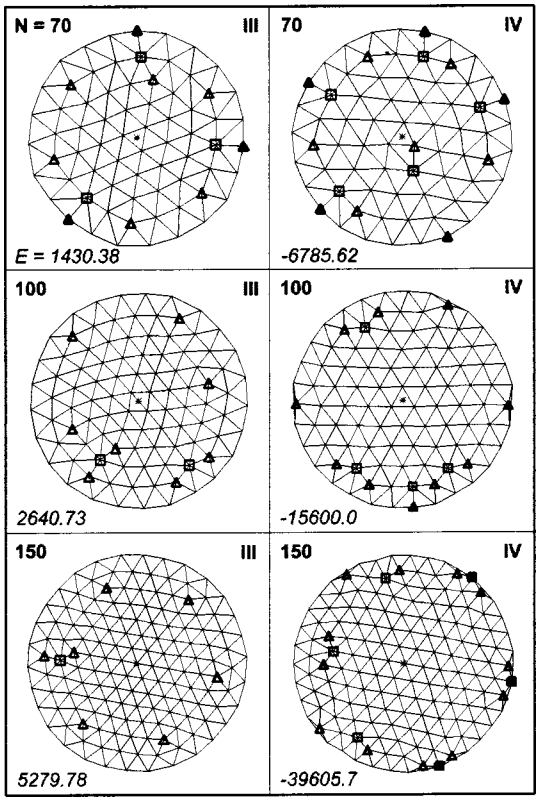

FIG. 6. A few typical configurations at $N=70$, 100, and 150 for the type-III and -IV interactions as defined in Table I. N and cluster energy are listed above and below each cluster, respectively.

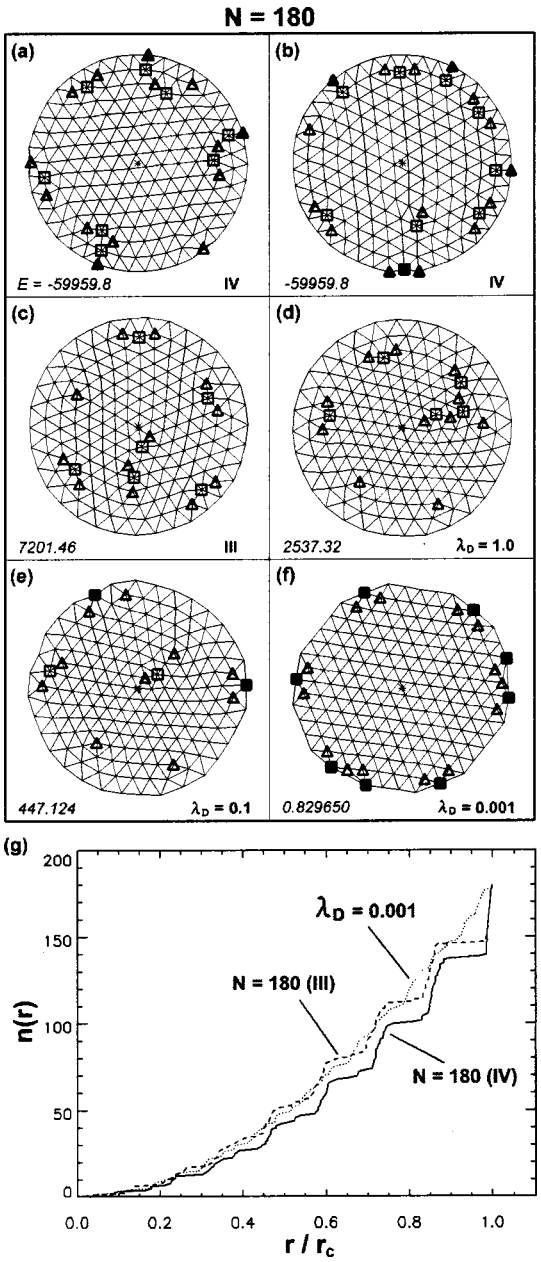

FIG. 7. (a)–(f) The typical configurations for $N=180$ and different interactions in a parabolic confining well. The dimensionless energy is listed below each cluster. The states in (a) and (b) have the same energy over the six digits but different defect configurations. Type-III and -IV interactions are defined in Table I. (d) and (e) are obtained with Yukawa-type interaction with $\lambda_D=1.0$, 0.1, and 0.001, respectively. (g) The radial distribution of $n(r)$, the cumulative number of particles inside a circle with radius r. r_c is the cluster radius for the clusters shown in (a), (c), and (f). The steeper steps for the outmost shells of the first two cases manifest the more distinguished outer circular shells.

sults with $V_{ij}=1/r_{ij}$ and $V_c r_i = r_i^2$ at $N=230$ [7]. The radial dependences of the mean lattice constant a_r at radius r are not the same when the form of the repulsion potential changes under the same parabolic confining potential. As shown in Fig. 9, for $V_{ij}=\ln(1/r_{ij})$, a_r remains almost constant when r/r_c and N change (where r_c is the cluster radius). However, for the Yukawa-type repulsion potential, it slowly increases with r in the inner triangular domain and drastically increases in the outer region. The mean lattice constant a averaged over the entire cluster decreases as N increases [Fig. 9(c)].

Similarly to the above small N clusters, each cluster is associated with -6 net topological charges. However, the smoother bending and the small ΔN_i for the outmost shell make most of the negative topological charges move inward from the outmost shell. Most of the defects appear around the boundary between the outer circular shells and the inner triangular domain. The fivefold defect smoothly bends the lattice lines about 60° around it and provides a smooth interface matching between the outer circular shell and the inner triangular domain (see all the isolated fivefold defects in Figs. 6–8). On the other hand, the free dislocation (i.e., the charge free 5-7 pair) mainly deteriorates the translational order but only slightly distorts long-range lattice orientation [18]. Around the corner of the inner hexagonal domain, the fivefold disclination is accompanied by a free dislocation to form a 5-7-5 defect, if the corner touches the adjacent outer circular shell [e.g., the 5-7-5 defects at the lower left part of the clusters in Fig. 7(c), where the third circular outmost shell merges with the piecewise straight fourth outmost shell]. It will stand alone if the touching does not occur. In addition to the above defects, the gradual lattice distortion caused by the slow change of a_r inside the inner triangular domain can be accommodated by a cluster (or clusters) of free dislocations stretching outward from the center of the inner domain with -1 net topological charge. It is also responsible for the gradual merging of the inner triangular lat-

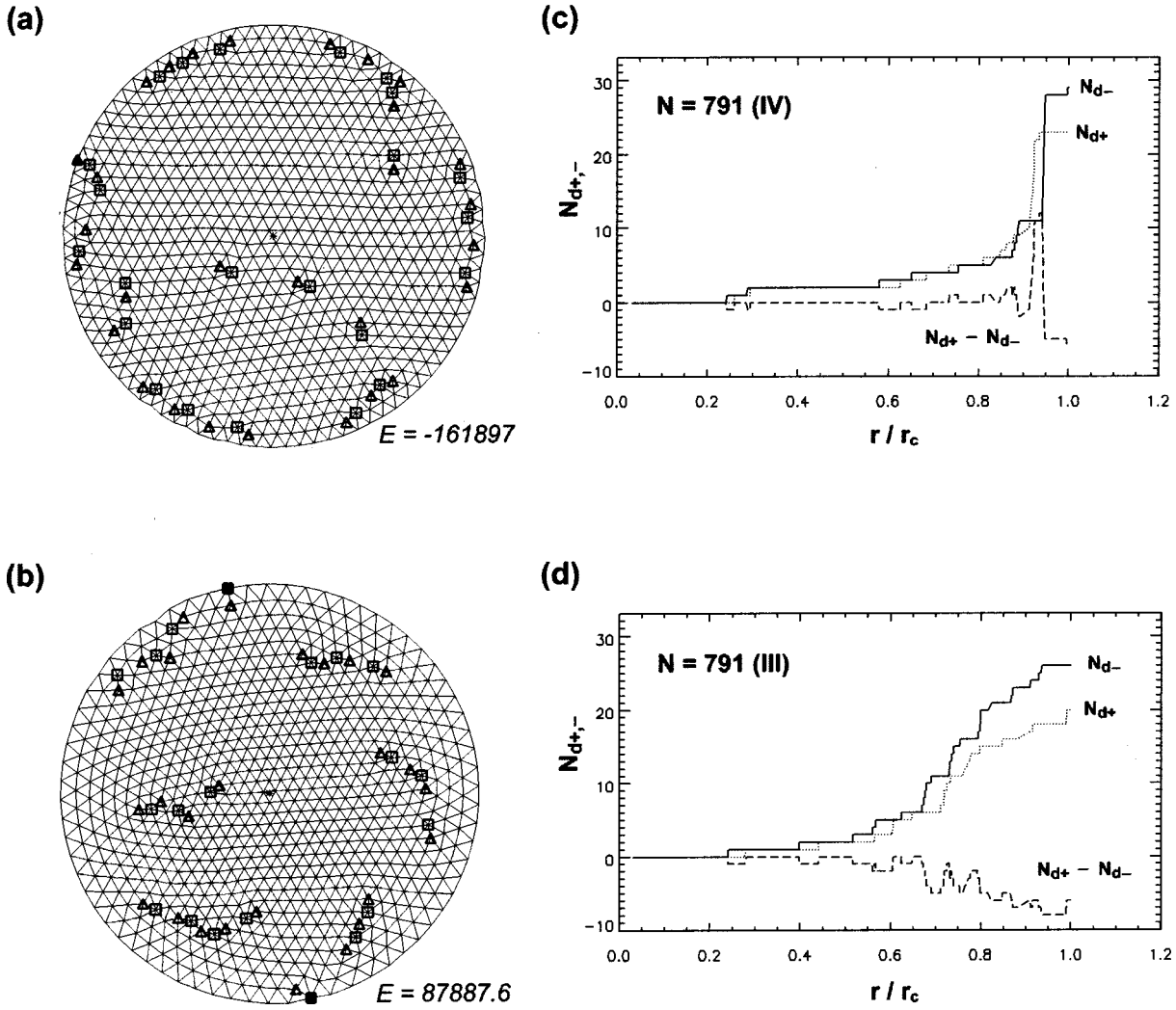

FIG. 8. (a) and (b) The packings and defects at particle number $N=791$ for the two typical cases with type-IV and -III interactions as defined in Table I, respectively. (c) and (d) The radial distribution of $N_{d+,-}(r)$, the cumulative numbers of the positive and negative topological defects, respectively, inside a circle with radius r, for the configurations in (a) and (b). The variations of $N_{d+}-N_{d-}$ are also plotted.

tice with piecewise straight boundaries and smoothly bent outer circular shells.

The above behavior can be clearly manifested in Figs. 6–8, which show examples for a series of different interactions with N from 70 to 791. For the configurations shown in Fig. 6 with N from 70 to 150, each inner core has a relatively defect-free triangular lattice due to the relatively uniform density. For $V_{ij}=\ln(1/r_{ij})$ at $N=180$ shown in Fig. 7(a), most of the defects are still expelled by the inner cores with almost uniform densities to the second and third outmost shells. The state shown in Fig. 7(b) has the same energy over six digits. The slight lattice readjustment associated with the isolated 5-7 defect pair present in the inner triangular domain further expels the defects from the third outmost shell. As the interaction range is shortened, e.g., under the Yukawa-type interaction shown in Figs. 7(c)–7(f), the cluster no longer has a uniform packing and the defects move inwards from the cluster boundary. For the Yukawa repulsion with $\lambda_D > 5$ and $N=180$ [Fig. 7(c)], each cluster has one fivefold defect, four 5-7-5 defects, and one cluster of fivefold and sevenfold defects stretching radially out from the center region. No nearly degenerate state with a defect-free inner triangular domain can be found. The topological structure remains similar even when λ_D is decreased to 1 [Fig. 7(d)]. The quite sharp stair-type accumulated particle number distribution at large r in Fig. 7(g) indicates that the cluster has two to three quite distinguished circular outmost shells. Figures 7(e) and 7(f) show that the further decrease of λ_D below 0.1 expels the defect outward to the two outmost shells. The outmost shell is no longer circular and becomes piecewise straight. The -6 topological charges are still conserved. The harder repulsive core at the small λ_D limit makes the system quite similar to the hard-sphere case. The triangular lattice with uniform packing density extends all the way to the outmost shell at $\lambda_D=0.001$. This trend is quite similar to the observation shown in Fig. 4 for the small N case. Similar argument of the competition between the strain energy associated with the defects and the confining energy can be used to explain the behavior. Note that unlike the small N cases shown in Fig. 4, where the hexagon-shaped outmost shell at small λ_D has six sharp corners, the six corners of the outmost shell shown in Fig. 7(g) are replaced by facets associated

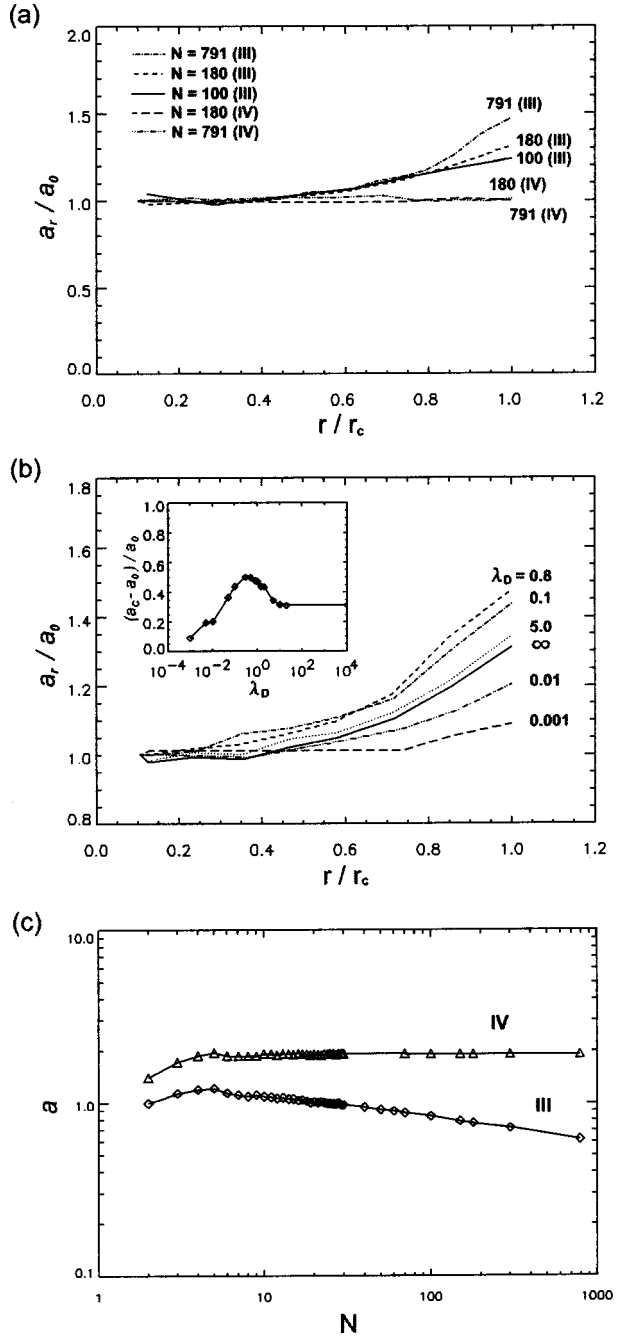

FIG. 9. (a) The radial variations of the lattice constant a_r normalized by the lattice constant a_0 at the cluster for the type-III and -IV potentials defined in Table I at $N=180$ and 791, where r_c is the radius of the cluster. (b) The normalized radial variations of lattice constant for the Yukawa interaction at different λ_D for the case of $N=180$. The inset shows $(a_c-a_0)/a_0$ vs λ_D, where a_c is the mean lattice constant at the cluster boundary (i.e., also the maximum a_r). (c) The mean lattice constant a vs N for the type-III and -IV interactions.

with four $-+-$ and two $-+--+$ defect clusters to reduce the confining potential.

Figure 8 shows the behavior at very large N ($N=791$). In Figs. 8(c) and 8(d), $N_{d+,-}(r)$, the numbers of the topological defect charges inside a circle with radius r are plotted. The cluster with $V_{ij}=1/r_{ij}$ shows several smooth circular outmost shells. There are more free dislocations (especially more extending to the inner triangular core) to accommodate the lattice distortion due to the nonuniform radial distribution of a_r. $N_{d+,-}$ and $N_{d+}-N_{d-}$ all have larger rises around $r/r_c=0.6$, where a_r also has a sharper rise [Fig. 9(a)]. For the case of $V_{ij}=\ln(1/r_{ij})$, the cluster has a more uniform packing density distribution (i.e., almost constant a_r). The triangular domain is less distorted than the case of $V_{ij}=1/r_{ij}$ and extends all the way to the outmost shell. It consequently has only a few free dislocations which have no net topological charge in the inner part. Only the outmost shell is circular. Unlike the type-III case, the defect clusters are mainly oriented azimuthally and accumulated along the piecewise circular second outmost shell, which is the interface between the circular shell and triangular domain [see the sharp rises of N_{d+} and N_{d-} and the large fluctuation of $N_{d+}-N_{d-}$ in this region shown in Fig. 8(d)]. The net topological charge of each cluster is still kept at -6.

The radial dependence of a_r and the variation of a under different interaction forms and N's shown in Fig. 9 can be easily understood from the point of force balance for each charged particle in the cluster. From the coarse-grained point, we can roughly estimate the force on a particle by accumulating the electric field from uniformly (azimuthally) charged rings for a circular symmetric confinement. The almost uniform lattice constant for the case of the $V_{ij}=\ln(1/r_{ij})$ potential corresponds to a uniform distribution of the coarse-grained charge density. Since the case of $\ln(1/r_{ij})$ repulsion potential is the ideal 2D case (i.e., from the uniformly charged infinite long wires), we can use a cylindrical Gauss surface to calculate the radial electric field. Only the uniform charge distribution can provide a parabolic potential to counterbalance the inward confining force. Namely, if we treat the parabolic V_c as being from a uniform neutralizing background, the coarse-grained charge distribution should also be uniform to null the space charge from the neutralizing background and reduce the total Hamiltonian. The discreteness of particles only makes higher-order correction on the packing density. To the zeroth-order approximation and under the circular symmetry, the charged particles outside the circle with radius r have no overall contribution on the electric forces for the particles at radius r. Therefore, increasing N does not affect the packing density and a [Figs. 9(a) and 9(c)]. The discreteness effect is stronger at small N, which causes the fluctuation of a as N changes. Certainly it is also not difficult to expect that the cluster will have higher packing density in the outer region, if we add a higher-order confining potential which corresponds to the higher neutralizing ion density in the outer region.

The case of $V_{ij}=1/r_{ij}$ corresponds to the interaction between two point charges on a 2D surface. We can no longer use a cylindrical Gauss surface. Using a coarse-grained picture, the radial electric field E at radius r generated by a uniformly charged ring at radius r' and with charge Q follows [19]:

$$E(r)=\frac{Q(r')}{4\pi\epsilon_0 r^2}\sum_{S=0}^{\infty}\left(\frac{(2S)!}{2^{2S}S!S!}\right)^2\left(\frac{r'}{r}\right)^{2S}$$

for $r>r'$ and

$$E(r)=\frac{-Q(r')}{4\pi\epsilon_0 r'^2}\sum_{S=0}^{\infty}\left(\frac{(2S)!}{2^{2S}S!S!}\right)^2\left(\frac{r}{r'}\right)^{2S}$$

for $r<r'$. The inner (outer) ring generates a radially outward (inward) force. Therefore, unlike the case of the $\ln(1/r_{ij})$ repulsion potential, the contributions from the particles in the outer rings have to be taken into account. In addition to the external confining force, the particles in the center region are further compressed to have higher density such that the higher outward electric field can be generated to reach the force balance. The particle density (lattice constant) thereby increases (decreases) as r decreases. When N increases, the particles in the center part certainly feel stronger inward repulsive force from the particles in the outer rings. It consequently causes the decrease of a [Fig. 9(c)] and the larger change of a_r/a_0 [Fig. 9(a)].

For the Yukawa-type interactions, the interaction range further shortens but with a steeper core as λ_D decreases. The charges on the outer rings also contribute a net inward radial electric force similar to the case with $V_{ij}=1/r_{ij}$ but with a faster decay as $|r-r'|$ increases. In addition to the radial confining force, the inward forces are only contributed from the charges on a few or even one adjacent outer ring for the small λ_D cases. Therefore, a_r also has a larger radial variation than the case with $V_{ij}=\ln(1/r_{ij})$.

It is interesting to point out that, similarly to the small N case, changing λ_D for $\lambda_D>2$ has very little effect on a_r (Fig. 5). The confining force compresses a to the range (between 0.6 and 0.85) smaller than λ_D, which makes the Yukawa interactions have similar forms at this distance. The mean lattice constant a equals λ_D at $\lambda_D=0.4$ for $N=180$. The decrease of a slows down as λ_D further decreases. For example, $a=0.25$ at $\lambda_D=0.1$. Also note that, under the competition between the linear confining force and the nonlinear Yukawa interaction, the percentage of variation of $a(r)$ reaches the maximum as λ_D approaches 1. Figure 9(b) shows that the variations of a_r/a_0, where a_0 is the lattice constant at the cluster center, are the same for $\lambda_D=0.5$ and 1.5, and $\lambda_D=0.1$ and 2.0.

IV. CONCLUSION

We investigate the packing of the 2D SCCC's in central confining potentials with various forms of repulsive interaction through MD simulations with annealing cycles to zero temperature. Generically, under the radial confining force, the concentric shells associated with the alternate periodic packing sequence in different shells for small N and the triangular lattice surrounded by circular shells at large N are observed regardless of the difference in the detailed interaction forms. The system also supports nearly degenerate metastable states with different combinations of occupation numbers or the same set of occupation numbers but different defect configurations (i.e., slightly different relative intershell particle positions). Each cluster has -6 net topological charges. Most of the negative topological charges stay on the cluster boundary for a small-N cluster. For a small-N cluster with more than two shells, the defects also appear in the inner region in the form of 5-, 5-7-5-, 7-5-7-, and 5-7-5-7-fold defects unless the inner region has a triangularly packed magic configuration. The competition between the strain energy from lattice deformation and the confining potential energy, which prefers a more circular structure with a smaller radius, causes the changes of the cluster shapes and the relative energies of the nearly degenerate states. The case with $V_{ij}=\ln(1/r_{ij})$ and parabolic V_c corresponds to the case with the ideal 2D Coulomb cluster in a uniformly charged neutralizing background. It supports a uniform particle density distribution to offset the coarse-grained background charges and balance the force on each particle. This causes the almost uniformly packed inner triangular lattice to extend nearly to the outmost circular shell for the clusters with large N. Steepening the confining well in the outer region increases the packing density in the outer region. Decreasing the interaction range causes the increasing packing density in the inner part, i.e., ΔN_i by one or two at small N and the increase of a_r with increasing r at large N. It also makes most of the topological charges move from the cluster boundary to the interface between the circular shells and the inner triangular domain for the interface matching, and some even extend to the inner triangular domain to accommodate the nonuniform lattice constant distribution at large N. This trend can be reversed at the very small λ_D limit, where under the hard-sphere-like interaction the system exhibits triangular packing throughout the cluster through expelling defects to the cluster boundary.

ACKNOWLEDGMENT

This research was supported by the National Science Council of the Republic of China under Contract No. NSC-88-2112-M008-008.

[1] H. Ikezi, Phys. Rev. Lett. **42**, 1688 (1979); P. Leiderer, W. Ebner, and V. B. Shikin, Surf. Sci. **113**, 405 (1982).
[2] *Nanostructure Physics and Fabrication*, edited by M. A. Reed and W. P. Kirk (Academic, Boston, 1989).
[3] D. Reefman and H. B. Brom, Physica C **183**, 212 (1991).
[4] W. I. Glaberson and K. W. Schwartz, Phys. Today **40** (2), 54 (1987).
[5] Y. Kondo *et al.*, Phys. Rev. Lett. **68**, 3331 (1992).
[6] J. J. Thomson, Philos. Mag. **39**, 236 (1904).
[7] V. M. Bedanov and F. M. Peeters, Phys. Rev. B **49**, 2667 (1994).
[8] V. A. Schweigert and F. M. Peeters, Phys. Rev. B **51**, 7700 (1995).
[9] A. A. Koulakov and B. I. Shklovskii, Phys. Rev. B **55**, 9223 (1997).
[10] Y. E. Lozovik and V. A. Mandelshtam, Phys. Lett. A **145**, 269 (1990); **165**, 465 (1992).
[11] B. Partoens and F. M. Peeters, J. Phys.: Condens. Matter **9**, 5383 (1997).
[12] L. Candido, J. P. Rino, N. Studart, and F. M. Peeters, J. Phys.: Condens. Matter **10**, 11 627 (1998).
[13] J. H. Chu and Lin I, Phys. Rev. Lett. **72**, 4009 (1994);

Lin I, W. T. Juan, and C. H. Chiang, Science **272**, 1626 (1996).
[14] G. E. Thomas *et al.*, Phys. Rev. Lett. **73**, 652 (1994).
[15] C. H. Chiang and Lin I, Phys. Rev. Lett. **77**, 647 (1996); W. T. Juan and Lin I, *ibid.* **80**, 3073 (1998).
[16] W. T. Juan, Z. H. Huang, J. W. Hsu, Y. J. Lai, and Lin I, Phys. Rev. E **58**, R6947 (1998); W. T. Juan, J. W. Hsu, Z. H. Huang, Y. J. Lai, and Lin I, Chin. J. Phys. **37**, 184 (1999).
[17] J. M. Liu, W. T. Juan, J. W. Hsu, Y. J. Lai, and Lin I, Plasma Phys. Controlled Fusion **41**, A47 (1999).
[18] J. Weertman and J. R. Weertman, *Elementary Dislocation Theory* (Oxford University Press, New York, 1992); K. J. Strandburg, *Bond-Orientational Order in Condensed Matter Systems* (Springer, New York, 1992).
[19] J. D. Jackson, *Classical Electrodynamics* (Wiley, New York, 1975).